

# **Seasonal Modulations and Propagation of Subantarctic Mode Water Potential Vorticity\***

Sunke Schmidt<sup>1</sup> and Gregory C. Johnson  
National Oceanic and Atmospheric Administration, Pacific Marine  
Environmental Laboratory, Seattle, Washington

*for Journal of Physical Oceanography*

submitted 18<sup>th</sup> October 2010

---

\* Pacific Marine Environmental Laboratory Contribution Number 3624

<sup>1</sup> *Corresponding author address:* Sunke Schmidt, National Oceanic and Atmospheric Administration,  
Pacific Marine Environmental Laboratory, 7600 Sand Point Way NE, Seattle, Washington 98115  
Email: [sunke.schmidt@noaa.gov](mailto:sunke.schmidt@noaa.gov)

## Abstract

Subantarctic Mode Water (SAMW) is formed in late austral winter along the northernmost front of the Antarctic Circumpolar Current (ACC), most prominently in the Indian and Pacific oceans. One distinctive feature of the SAMW is its annually renewed pycnostad, a pronounced potential vorticity ( $\bar{\omega}$ ) minimum that distinguishes the SAMW from surrounding water masses. After subduction SAMW spreads northward, ventilating mid-depth subtropical and tropical waters at the base of the permanent pycnocline. Here the seasonal evolution of SAMW  $\bar{\omega}$  structure is analyzed using data from the Argo array of freely drifting, profiling CTD floats. The core potential density anomaly of the SAMW pycnostad increases from west to east, from  $\sigma_\theta = 26.68 \text{ kg m}^{-3}$  in the western Indian Ocean to  $27.0 \text{ kg m}^{-3}$  around Drake Passage. Seasonal  $\bar{\omega}$  anomalies of amplitude  $\sim 4 \times 10^{-12} \text{ m}^{-1} \text{ s}^{-1}$  within the SAMW propagating at phase speeds of  $2.5$  to  $10 \text{ cm s}^{-1}$  on five core isopycnals spanning SAMW in the Indian and Pacific oceans. These phase speeds significantly exceed current velocities estimated on these isopycnals by combining direct velocities from Argo float displacement data with geostrophic estimates from Argo density data. Phase speeds are lowest at midlatitudes and increase towards the equator when roughly following streamlines of the velocity field. These  $\bar{\omega}$  anomalies could be thought of as 2<sup>nd</sup> baroclinic mode structures, and exhibit phase propagation similar to predictions for these modes.

# 1. Introduction

Subantarctic Mode Water (SAMW; McCartney 1977) is a thick layer of water with vertically relatively homogenous properties (hence a mode) found equatorward of the northernmost front of the Antarctic Circumpolar Current (ACC), the Subantarctic Front (SAF), in the Southern Hemisphere. Varieties of SAMW are subducted at the southern edges of the subtropical gyres, and move generally northward and westward, ventilating the bases of the Southern Hemisphere subtropical thermoclines (Hanawa and Talley 2001). The formation and subduction of SAMW arises from a complicated interplay among winter-atmospheric buoyancy loss, northward Ekman transport, lateral induction, and eddy processes (Rintoul and England 2001, Karstensen and Quadfasel 2002, Salle et al. 2006, 2010, Koch-Larrouy 2010).

Perhaps the most prominent structure found in all varieties of SAMW is a pycnostad (Seitz 1967), a thick layer of relatively vertically uniform density (McCartney 1977). This structure is strongest just north of the SAF, diminishing to the north, but distinct to about 20°S in places, north of which it is completely eroded. This pycnostad corresponds by definition to a local vertical extremum in planetary potential vorticity,  $\Pi = f/\rho (\partial\rho/\partial z)$ , where  $f$  is the Coriolis parameter,  $\rho$  is potential density referenced to the central depth over which its vertical gradient is estimated, and  $z$  is depth. This quantity has the advantage of being conserved in inviscid geostrophic flows (Pedlosky 1987). While  $\Pi$  is negative in the Southern Hemisphere, henceforth when we refer to the vertical minimum of this quantity in the SAMW, we have its absolute value in mind.

As mentioned above, a complex interaction of processes lead to SAMW formation and subduction. Nonetheless, subduction itself is fundamentally tied to the seasonal cycle, imparting a strong signature of the densest (and thickest) late-winter mixed-layer properties to the water mass being subducted (Stommel 1979). After subduction, conservative water mass properties including  $\sigma_t$  would be preserved in an inviscid flow (Pedlosky 1987), but are in reality modified by mixing processes. For all varieties of SAMW the low core values of  $\sigma_t$ , being local vertical and lateral extrema, will erode (increase in magnitude) with distance in space and time from their creation. Furthermore, one might expect some seasonal modulation of SAMW properties as the large-scale circulation of the subtropical gyres continues year-round while SAMW subduction is predominantly a late-winter phenomenon.

Here we study seasonal modulations of  $\sigma_t$  within the SAMW of the Indian and Pacific oceans using hydrographic and velocity data from the Argo array of profiling CTD floats (Roemmich et al. 2009). We focus on the spreading and propagation of these anomalies in  $\sigma_t$  downstream from the regions where SAMW is subducted. (In the Atlantic Ocean the data distribution, a complex circulation, and the generally sparse low  $\sigma_t$  waters around the Atlantic SAMW confound the analysis.) We find the phase speeds of the anomalies in our monthly isopycnal climatology somewhat exceed our estimates of the advective velocities of the large-scale circulation, similar to theoretical predictions for the phase speed of subsurface thickness anomalies (Thompson and Ladd 2004) which are identified as 2<sup>nd</sup> baroclinic mode.

## 2. Data and methods

We use all available quality-controlled Argo float data downloaded from an Argo Global Data Assembly Center in March 2010. We restrict our analysis to data flagged as good (quality flag 1). Delayed-mode data are used as available, otherwise real-time data are used. For individual float profiles potential temperature ( $\theta$ ), salinity (S) and pressure (P) are interpolated onto potential density anomaly ( $\sigma_\theta$ ) levels at  $0.02 \text{ kg m}^{-3}$  intervals.

During this process, salinity and pressure data that lie outside 3 times the interquartile range relative to the first and third quartiles within local bins are also rejected as extreme outliers.

On each isopycnal level we map these quantities (regardless of year) onto a 1 month  $\times$   $1^\circ$  lat.  $\times$   $1^\circ$  long. climatological grid using a LOESS filter. The temporal cut-off radius of the filter is three months and the horizontal radii are adaptive. The zonal radius is twice that of the meridional radius owing to the strong zonal nature of features in the interior of the Southern Ocean, although this choice slightly distorts the mapped fields near eastern and western boundaries. The mapping uses the closest 2800 data points, with a lower threshold for the meridional cut-off radius of  $3.5^\circ$  lat., expanding to an upper threshold of  $7.5^\circ$  as necessary to reach (or in very data-sparse regions, approach) the 2800 data point target. Grid points in the climatology that have a sum of all weights  $< 100$  or a LOESS-weighted distance from the grid point more than 0.8 times the maximum cut-off radius are removed.

We calculate  $\Pi$  for each grid point at  $0.02 \text{ kg m}^{-3}$  intervals (between each pair of  $\sigma_\theta$  levels). Geostrophic current calculations are done on a 2-dbar pressure grid referenced to a 1000 db zero-velocity surface and linearly interpolated onto the center of each  $\Pi$

isopycnal range. We make the referenced geostrophic velocities absolute by using a velocity field constructed from the 1000-dbar float displacements in the YoMaHa raw data set (Lebedev et al. 2007), again as downloaded in March 2010. We apply the same mapping scales and technique to these displacement data as for the isopycnal float climatology, but generating a single mean (data mapped regardless of date), hence assuming little seasonal flow variability at 1000 dbar.

Isopycnal climatologies like that which we analyze here better represent water-properties than isobaric ones, especially near strong fronts like the Gulf Stream or the ACC (Lozier et al. 1994). This improved representation is crucial for the SAMW, with its strong meridional isopycnal slopes and water-property gradients. We make no attempt to join the subsurface (ocean interior) isopycnal climatology we construct here to a mixed layer. This neglect is acceptable as we are focusing only on processes and properties of SAMW following subduction along isopycnals.

### 3. SAMW structure

Properties at the core of the SAMW, defined as the vertical minimum in  $\bar{w}$  below the seasonal pycnocline and shallower than 800 m, vary significantly spatially (Fig. 1). We limit our analysis to areas with  $|\bar{w}| < 50 \times 10^{-12} \text{ m}^{-1} \text{ s}^{-1}$ , a fairly stringent limit. The values of  $\sigma_\theta$  at the SAMW core (Fig. 1a, black lines) near the ACC are lightest in the southwestern Indian Ocean ( $26.65 \text{ kg m}^{-3}$ ) and trend progressively denser towards the east, finally reaching their densest value ( $27.2 \text{ kg m}^{-3}$ ) in the southwestern Atlantic Ocean. Core values of  $\theta$  (Fig. 1a, white lines) drop monotonically from  $12^\circ\text{C}$  to  $4^\circ\text{C}$  and of  $S$  (Fig. 1b, white lines) from 35.2 to 34.2 PSS-78 over the same geographical range,

hence the cooling counteracts and dominates the freshening to increase the density at the SAMW core progressing eastward from the southwestern Indian Ocean.

Values of the  $\Pi$  minimum (Fig. 1b, colors) at the SAMW core also vary spatially. The lowest values are generally found just north of the ACC, and magnitudes increase to the north. However, there are east-west variations as well. The lowest values are found south of Australia and in the central and eastern South Pacific Ocean, areas previously identified as specific SAMW formation regions (e.g. Salle et al. 2010). The values in the Atlantic are relatively high; the SAMW signal there is less clear. No values fall below our upper limit in the western parts of the Indian and Pacific oceans, where the Agulhas and East Australia western boundary currents of the subtropical gyres introduce more stratified subtropical waters from the north. The region with the thickest  $|\Pi| < 50 \times 10^{-12} \text{ s}^{-1} \text{ m}^{-1}$  layer (Fig. 1a, colors) is the Southwest Pacific, between the regions of lowest core  $\Pi$ , suggesting that the location with the most SAMW is not necessarily a primary formation region.

The depth of the core  $\Pi$  values (Fig. 1b, black lines) generally deepens to the north. This pattern occurs because of the erosion of the core from above by more stratified subtropical waters to the north. This hypothesis is supported by the increase of the density of the core  $\Pi$  values (Fig. 1a, black lines) and the increase of the magnitude of the core  $\Pi$  values (Fig. 1b, colors), to the north.

A quasi-zonal vertical section of  $\Pi$  (Fig. 1c, colors) with  $\sigma_\theta$  (Fig. 1c, black lines) constructed following the meridional minimum in core SAMW  $\Pi$  values just north of the SAF and within the subduction regions (Fig. 1c, red line near top with gray continents for orientation) allows another perspective on the varieties and zonal evolution of SAMW

just discussed. Distinct pools of SAMW of differing properties south of Australia, the Tasman Sea, the central South Pacific, and the eastern South Pacific are apparent. The radically different nature of the densest  $\sigma_t$  minimum in the South Atlantic is also clear.

#### 4. Seasonal modulation of the $\sigma_t$ minimum

As mentioned above, one might expect some seasonal modulation of SAMW properties given that SAMW subduction is an annually recurring, predominantly late-winter phenomenon. Imagine a recurring seasonal cycle with no interannual variability and a steady gyre circulation. One would expect a seasonal modulation of the  $\sigma_t$  minimum at the core of SAMW near its formation region, with lower absolute values in late winter. This modulation, in combination with steady advection away from the formation region by the general circulation, would result in a propagation of low  $\sigma_t$  anomalies downstream of the region, appearing schematically like proverbial  $\sigma_t$  anomaly pigs in a SAMW python (Fig. 2). At any given point downstream these passing anomalies would be manifested locally as an annual modulation of  $\sigma_t$  within the SAMW.

We fit an annual harmonic to the monthly  $\sigma_t$  values at each location to better determine the month in which the  $\sigma_t$  value reaches its smallest magnitude there. This approach guards against classifying a  $\sigma_t$  spike towards small magnitude in a single month arising from noise as the month of the minimum. However, selecting the month with the minimum magnitude instead of using the harmonic analysis does not significantly alter the resulting maps of  $\sigma_t$  minimum phase visually. Depending on the isopycnal, 30-40% of the data within grid points have a correlation with the annual harmonic above 0.8, with fewer grid points in each successive correlation bin below 0.8 (Fig. 3). All isopycnals have fewer than 25% of grid points with a correlation of 0.5 or less.



The month of the local  $II$  minimum within the SAMW (Fig. 4, left panels, colors) shows fairly distinct banded patterns oriented roughly perpendicular to the geostrophic flow (white arrows) on five different isopycnals: two in the Indian and three in the Pacific Ocean. Magnitudes of  $II$  (Fig. 4, left panels, black contours) are generally lowest to the south near the SAMW origins and increase with distance from the source. The aggregate of local de-measured annual variations of  $II$  aligned by the months of their maximum values (Fig. 4, right panels) illustrates again the robust annual cycle of  $II$  within the SAMW (see also Fig. 3). We discuss these patterns in more detail below.

#### *a. Indian Ocean*

We select two isopycnals to discuss Indian Ocean SAMW:  $\sigma_\theta = 26.68 \text{ kg m}^{-3}$  and  $26.78 \text{ kg m}^{-3}$  (Fig. 4a - d). These surfaces illustrate the lightest and densest SAMW varieties that fully lie within the Indian Ocean west of Australia and span a significant area. The area of low magnitude  $II$  SAMW with  $\sigma_\theta < 26.68 \text{ kg m}^{-3}$  is marginal (Fig. 1a, colors). We do not discuss further the significant amount of SAMW with  $\sigma_\theta > 26.78 \text{ kg m}^{-3}$  that is formed and stays mainly south of Australia (Fig. 1c, black contours) or is found very close to the Leeuwin Current just offshore of the west coast of Australia, where it is only suboptimally resolved by this climatology because of the long zonal scales used in its construction.

The spatial pattern of months of the local annual  $II$  minima for the lighter Indian Ocean SAMW on  $\sigma_\theta = 26.68 \text{ kg m}^{-3}$  (Fig. 4a, colors) clearly reveals broad bands of phase propagating northwestward. This phase propagation of  $II$  minimum is also present for the denser Indian Ocean SAMW on  $\sigma_\theta = 26.78 \text{ kg m}^{-3}$  (Fig. 4c, colors), but is not very clear near the SAMW origin in the southeastern Indian Ocean. Still, most grid points on

this denser surface do have a pronounced annual  $\Pi$  cycle (Fig. 4b vs. d). In addition, on  $\sigma_\theta = 26.78 \text{ kg m}^{-3}$  low  $\Pi$  SAMW spreads nearly over the entire subtropical gyre and has mostly substantially lower  $\Pi$  magnitudes than on  $\sigma_\theta = 26.68 \text{ kg m}^{-3}$  (Figs. 1a, b, 4a, c). This denser isopycnal deepens significantly east and northward around the southwestern tip of Australia, which might be a reason for an absence of phase propagation pattern south of  $32^\circ\text{S}$ . Again, phase propagation is clearer from  $32^\circ\text{S}$  northward on this denser isopycnal.

The rate of phase propagation is nicely revealed by Hovmöller analysis (Fig. 5a, b) along paths roughly following geostrophic currents (Fig. 4a, c, gray lines with 1000-km distance stamps). The analysis suggests a  $\Pi$  anomaly propagation speed of  $\sim 5 \text{ cm s}^{-1}$  north of  $35^\circ\text{S}$  for SAMW on  $\sigma_\theta = 26.78 \text{ kg m}^{-3}$ . In general,  $\Pi$  anomalies appear to propagate within SAMW along both Indian Ocean surfaces ( $\sigma_\theta = 26.68 \text{ kg m}^{-3}$  and  $26.78 \text{ kg m}^{-3}$ ) with a phase speed of  $\sim 5 \text{ cm s}^{-1}$  south of  $30^\circ\text{S}$  and  $\sim 7.5 \text{ cm s}^{-1}$  northward of that latitude (Fig. 5a, b) as suggested by the clearly visible northwestward spreading  $\Pi$  bands (Fig. 4a, c).

### *b. Pacific Ocean*

We choose three isopycnals that span the Pacific Ocean SAMW from west to east (Fig. 4e–k):  $\sigma_\theta = 26.88 \text{ kg m}^{-3}$ ,  $26.94 \text{ kg m}^{-3}$ , and  $26.98 \text{ kg m}^{-3}$ . The lightest surface,  $\sigma_\theta = 26.88 \text{ kg m}^{-3}$ , falls within the region of thickest vertical levels of SAMW (Fig. 1a) despite the absence of a pronounced low  $\Pi$  core there (Fig. 1c). The denser surfaces,  $\sigma_\theta = 26.94 \text{ kg m}^{-3}$  and  $26.98 \text{ kg m}^{-3}$ , are close to or at the two  $\Pi$  minimums in the central and eastern South Pacific (Fig. 1b) respectively, and low  $\Pi$  SAMW on these surfaces reaches all the

way to the west Pacific. Furthermore, low  $II$  SAMW on  $\sigma_\theta = 26.98 \text{ kg m}^{-3}$  covers the largest area of SAMW on all isopycnal levels considered.

The month of the annual minimum in  $II$  anomaly on these isopycnals in the Pacific Ocean (Fig. 4e, g, i) reveals banded patterns similar to those found in the Indian Ocean. Again, these patterns of  $II$  anomaly bands on all isopycnals suggest north and northwestward phase propagation. Furthermore,  $II$  anomaly cycles of similar amplitude are observed for  $\sigma_\theta = 26.94 \text{ kg m}^{-3}$  and  $26.98 \text{ kg m}^{-3}$  within the SAMW low  $II$  regions (Fig. 4h, k). A slightly stronger seasonality of  $II$  anomaly is seen for  $\sigma_\theta = 26.88 \text{ kg m}^{-3}$  within the SAMW (Fig. 4f), despite the less pronounced core (higher  $II$ ) values.

A Hovmöller analysis along two approximate geostrophic flow pathways on isopycnals (Fig. 4c, d) in the central ( $\sigma_\theta = 26.94 \text{ kg m}^{-3}$ ) and eastern ( $\sigma_\theta = 26.98 \text{ kg m}^{-3}$ ) South Pacific suggest  $II$  anomaly propagation velocities of  $\leq 2.5 \text{ cm s}^{-1}$  south of  $35^\circ\text{S}$  for SAMW in the central South Pacific (on  $\sigma_\theta = 26.94 \text{ kg m}^{-3}$ ) and south of  $40^\circ\text{S}$  for SAMW in the eastern South Pacific (on  $\sigma_\theta = 26.98 \text{ kg m}^{-3}$ ). North of these latitudes the phase propagation of  $II$  anomalies appears to be considerably faster.

Animations (not shown) of  $II$  anomaly seasonal cycles on  $\sigma_\theta = 26.94 \text{ kg m}^{-3}$   $26.98 \text{ kg m}^{-3}$  suggest a cyclonic-phase propagation roughly following the outer isovorts of the SAMW considered here. While this pattern is not obvious in the Hovmöller analysis (Fig. 5c, d) or in the maps of the month of minimum  $II$  anomaly on isopycnals (Fig. 4g, i), it is discussed further below.

## 5. Geostrophic spreading

Since SAMW is arguably the most prominent upper-ocean water mass in the Southern Hemisphere we are interested in its residence times and propagation patterns. Knowing more about the flow patterns within SAMW can help understanding its role in ventilating waters below the thermocline, both isopycnally and via diapycnal mixing. We use geostrophic current estimates to compare observed  $\eta$  anomaly propagation with a dynamically derived flow field (Fig. 4, left panels, white arrows).

The flow fields we use in our analysis are calculated using monthly geostrophic velocities estimated at 2-dbar pressure intervals and interpolated onto isopycnals. These flow fields are made absolute using estimates of the velocity at 1000 dbar derived from float displacement data as explained above.

### *a. Indian Ocean*

Geostrophic currents are similar for both Indian Ocean isopycnals considered here (Fig. 4, left panels, white arrows): northwest turning westward and with increasing velocities from south to north. The northern end of the eastward-flowing AAC is obvious only south of  $45^\circ\text{S}$  on  $\sigma_\theta = 26.78 \text{ kg m}^{-3}$  (Fig. 4c), with a rapid transition into northwestward flow immediately north of the ACC. Geostrophic currents are generally orthogonal to bands of  $\eta$  anomalies with similar minimum months, as might be expected dynamically (except perhaps west of the southwestern tip of Australia).

### *b. Pacific Ocean*

All Pacific isopycnals share a geostrophic current feature close to the Eltanin Fracture Zone (about  $130^\circ\text{W}$   $54^\circ\text{S}$  – Smith and Sandwell, 1997) of the East Pacific Rise,

which extends as shallow as 750 m in this region. Here the ACC diverts temporarily northward within the SAMW (Fig. 4e, g, i), with apparently wide-reaching effects on the geostrophic flow and perhaps the SAMW distribution. Around 130°W one branch of the geostrophic flow field turns northward over a fairly wide longitude range while another branch continues in a more northeasterly direction on the other side of the East Pacific Rise. The influence of the rise is also apparent in the SAMW thickness minimum (Fig. 1a) and east-west sloping isopycnals, as well as the different core densities of SAMW on either side of the rise (Fig. 1c). On  $\sigma_\theta = 26.88 \text{ kg m}^{-3}$  areas with  $II$  below the low SAMW threshold used here are only found west of this location (Fig. 4e), while  $\sigma_\theta = 26.94 \text{ kg m}^{-3}$  (Fig. 4g) and  $\sigma_\theta = 26.98 \text{ kg m}^{-3}$  SAMW (Fig. 4i) low  $II$  areas span both the Southeast Pacific and Southwest Pacific basins. While the isopycnal in the western South Pacific SAMW (Fig. 4e,  $\sigma_\theta = 26.88 \text{ kg m}^{-3}$ ) shows mainly the northwest branch of this South Pacific flow field, the other denser isopycnals (Fig. 4g, i) show northwest currents in the west and northeast currents in the east between 50°S and 35°S. The current directions fan around the Eltanin Fracture Zone. The mid-latitude geostrophic currents have higher northward velocities in the east than in the west. North of 35°S currents on all isopycnals accelerate into a westward flow band—the northern limb of the subtropical gyre (Fig. 4e, g, i).

## 6. Discussion and Conclusions

Our analysis concentrates on several varieties of SAMW found in the Indian and Pacific oceans, examining properties and flow fields on isopycnals spanning the low  $II$  cores of

these varieties. We focus on the obvious northward and northwestward-moving annual cycle in  $\Pi$  anomalies on all isopycnals analyzed (Fig. 4, left panels). These patterns suggest, as might be expected, that seasonal  $\Pi$  propagation after subduction is to a large degree similar each year. Erratic short time-scale or interannually varying SAMW pathways and core properties would work to obscure the  $\Pi$  phase pattern so apparent in the monthly climatology presented here, thus seasonal processes appear to dominate.

The most obvious  $\Pi$  anomaly phase propagation pattern for an entire isopycnal within the low  $\Pi$  SAMW core stands out in the western Indian Ocean SAMW on  $\sigma_\theta = 26.68 \text{ kg m}^{-3}$  (Fig. 4a). All other surfaces also include areas with less obvious phase propagation patterns (Fig. 4, other left panels). However, the Hovmöller analysis (Fig. 5) does suggest propagation throughout these isopycnals with lower amplitudes in the interior regions of each isopycnal and elevated amplitudes at the creation region and at the boundary closer to the SAMW limit of  $|\Pi| = 50 \times 10^{-12} \text{ m}^{-1} \text{ s}^{-1}$  used here. The reasons for the less obvious propagation patterns in the interior regions on some isopycnals analyzed here are uncertain, but several factors may contribute. One strong possible explanation is that in regions where geostrophic currents are very slow, the horizontal wavelength for seasonal  $\Pi$  anomalies may approach or fall below the threshold that can be resolved by the mapping scales used to construct the climatology. There does appear to be a correlation between mapped geostrophic currents and the seasonal  $\Pi$  anomaly phase and amplitude: regions with higher geostrophic velocities show stronger amplitudes and thus have a higher signal-to-noise ratio (Figs. 4, left panels, and 5). This hypothesis is further supported by the fact that  $\Pi$  anomaly amplitude on the Indian Ocean isopycnals does not show the pronounced drop in amplitude in the center as in the Pacific

while having geostrophic currents exceeding those in the Pacific Ocean. Alternately, a slower and less well-aligned flow field, as found in the interior of most surfaces studied, could also create convergence or divergence in  $\Pi$  anomaly phase propagations and thus obscure any obvious patterns. Finally,  $\Pi$  phase propagation on under- or overlying SAMW surfaces might cause isopycnal displacements that interfere with  $\Pi$  phase on the surfaces analyzed.

The amplitude of the seasonal  $\Pi$  cycle (Fig. 4, right panels) only approaches  $8 \times 10^{-12} \text{ m}^{-1} \text{ s}^{-1}$  and is less for the majority of grid points. With only  $\Pi$  values below  $50 \times 10^{-12} \text{ m}^{-1} \text{ s}^{-1}$  analyzed, a conservative estimate of the annual  $\Pi$  cycle on each grid point is on the order of 10% of the mean, the ratio being somewhat higher close to the subduction region where lower mean  $\Pi$  values are found (Figs. 1b, 4, right panels, and 5) and at the boundaries where the cycle amplitude is large. We do not find a simple correlation between  $\Pi$  and annual  $\Pi$  cycle amplitude. Possible reasons for the smaller amplitude in the annual  $\Pi$  cycle in the interior regions of isopycnals studied (Figs. 4 and 5) are discussed above. We leave investigation of the apparent amplitude changes in the seasonal  $\Pi$  anomalies along their propagation paths to the future.

All analyzed SAMW density surfaces show a propagation of  $\Pi$  phase. To verify whether the  $\Pi$  propagation corresponds to water mass displacements, we calculate geostrophic currents and superimpose them. For the geostrophic flow and  $\Pi$  phase propagation speeds to be similar on the isopycnals analyzed, the 2-year current displacement vectors shown (Fig. 4, left panels, white arrows) would need to span two complete wavelengths of  $\Pi$  seasonal cycles. This criterion is not met on any of the

isopycnals shown. The discrepancy is such that  $\Pi$  anomaly phase speeds significantly exceed the speeds of geostrophic currents.

Geostrophic currents show northward speeds of  $< 1 \text{ cm s}^{-1}$  close to the formation region, north of the ACC (Fig. 4g, i), increasing up to  $\sim 3 \text{ cm s}^{-1}$  in the subtropical Pacific Ocean and up to  $\sim 5 \text{ cm s}^{-1}$  in the subtropical Indian Ocean (Fig. 4, left panels). In general, these geostrophic flows appear to be orthogonal to bands of constant  $\Pi$  anomaly phase, so the phase propagation is aligned with the geostrophic flow. However, the phase propagation speeds for  $\Pi$  anomalies are  $\leq 2.5 \text{ cm s}^{-1}$  close the ACC in the Pacific Ocean increasing to  $\sim 5 \text{ cm s}^{-1}$  northward (Fig. 5c, d) and  $> 7.5 \text{ cm s}^{-1}$  in the Indian Ocean (Fig. 5a, b). The phase speeds for  $\Pi$  anomaly propagation appear to exceed the geostrophic flow on all isopycnals. Subtracting the geostrophic displacements from these observed phase speeds should yield the approximate wave propagation speeds for a resting ocean. These differences are on the order of  $1 \text{ cm s}^{-1}$  around  $50^\circ\text{--}40^\circ\text{S}$  increasing to the order of  $2\text{--}3 \text{ cm s}^{-1}$  in subtropical regions. These wave velocities are close to the westward-propagating baroclinic 2<sup>nd</sup> mode speeds for a resting ocean as calculated by Thompson and Ladd (2004) modeling disturbances in the North Pacific Ocean.

Since the annual formation of SAMW along the northern rim of the ACC can be seen as disturbance and water mass displacement by geostrophy can only explain a fraction of the seasonal  $\Pi$  anomaly movement, it seems likely that the observed phase propagations are indeed the 2<sup>nd</sup> vertical mode waves, observed here in Argo data.

We mostly neglect the lowest  $\Pi$  SAMW south of Australia (Fig. 1b, c) and the portion of the eastern South Pacific SAMW that is exported to the South Atlantic via the Drake Passage. This first neglect is partly justified by the fact that SAMW south of



Australia is of similar or lesser thickness than in the Indian and Pacific oceans (Fig. 1a, c) and at the same time has very limited northward extent. Thus SAMW found south of Australia fills a significantly smaller volume than the other analyzed varieties. The very low  $II$  values of SAMW found south of Australia may be explained by annual renewal without significant northward propagation. This climatology would be pushed beyond its limit by a thorough analysis of this variety close to the several narrow topographic and current features, including the ACC, mainland Australia, Tasmania, and New Zealand. Secondly, the same limitations would apply to the case of the far eastern Pacific SAMW exported to the Atlantic in terms of Tierra del Fuego, the Falklands, and the ACC, which is in any event quite distinct (Fig. 1c) from the varieties analyzed here.

#### *Acknowledgments.*

Float data used here were collected and made freely available by Argo (<http://www.argo.net/>), a program of the Global Ocean Observing System, and contributing national programs. The NOAA Climate Program Office and the NOAA Office of Oceanic and Atmospheric Research supported this research. The findings and conclusions in this article are those of the authors and do not necessarily represent the views of the National Oceanic and Atmospheric Administration.

## References

- Hanawa, K., and L. D. Talley, 2001: Mode Waters. In *Ocean Circulation and Climate: Observing and Modelling the Global Ocean*, Siedler, G., J. Church, and J. Gould eds., Academic Press, San Diego, 373–386.
- Karstensen J., and D. Quadfasel, 2002: Formation of Southern Hemisphere thermocline waters: Water mass conversion and subduction. *J. Phys. Oceanogr.*, **32**, 3020–3038.
- Koch-Larrouy A., R. Morrow, T. Penduff, and M. Juza, 2010: Origin and mechanism of Subantarctic Mode Water formation and transformation in the southern Indian Ocean. *Ocean Dynam.*, **60**, 563–583.
- Lebedev K., H. Yoshinari, N. A. Maximenko, and P. W. Hacker, 2007: *YoMaHa'07: Velocity data assessed from trajectories of Argo floats at parking level and at the sea surface*. IPRC Technical Note No. 4(2), 16 pp.
- Lozier, M. S., M. S. McCartney, and W. B. Owens, 1994: Anomalous anomalies in averaged hydrographic data. *J. Phys. Oceanogr.*, **24**, 2624–2638.
- McCartney M. S., 1977: Subantarctic Mode Water. In “*A Voyage of Discovery: George Deacon 70<sup>th</sup> Anniversary Volume (supplement to Deep–Sea Res.)*”, M. V. Angel, ed., Pergamon Press, Oxford, 103–119.
- Pedlosky, J., 1987: *Geophysical Fluid Dynamics*. Springer–Verlag, New York, 2nd ed., 710 pp.
- Rintoul R.R., and M. H. England, 2001: Ekman transport dominates local air-sea fluxes in driving variability of Subantarctic Mode Water. *J. Phys. Oceanogr.*, **32**, 1308–1321.

- Roemmich, D., G. C. Johnson, S. Riser, R. Davis, J. Gilson, W. B. Owens, S. L. Garzoli, C. Schmid, and M. Ignaszewski, 2009: The Argo Program: Observing the global ocean with profiling floats. *Oceanography*, **22** (2), 34–43.
- Sallee, J. B., N. Wienders, K. Speer, and R. Morrow, 2006: Formation of subantarctic mode water in the southeast Indian Ocean. *Ocean Dynam.*, **56**, 525–542.
- Sallee, J. B., K. Speer, R. Rintoul, and S. Wijfels, 2010: Southern Ocean thermocline ventilation. *J. Phys. Oceanogr.*, **40**, 509–529.
- Seitz, R. C., 1967: Thermostad, the antonym of thermocline. *J. Mar. Res.*, **25**, 203.
- Sloyan, B. M., L. D. Talley, T. K. Chereskin, R. Fine, and J. Holte, 2010: Antarctic Intermediate Water and Subantarctic Mode Water formation in the southeast Pacific: The role of turbulent mixing. *J. Phys. Oceanogr.*, **40**, 1558–1574.
- Smith, W. H. F., and D. T. Sandwell, 1997: Global seafloor topography from satellite altimetry and ship depth soundings. *Science*, **277**, 1957–1962.
- Stommel, H., 1979: Determination of water mass properties of water pumped down from the Ekman layer to the geostrophic flow below. *Proc. Natl. Acad. Sci.*, **76**, 3051–3055.
- Thompson L., and C. A. Ladd, 2004: The response of the North Pacific Ocean to decadal variability in atmospheric forcing: Wind versus buoyancy forcing. *J. Phys. Oceanogr.*, **34**, 1373–1386.

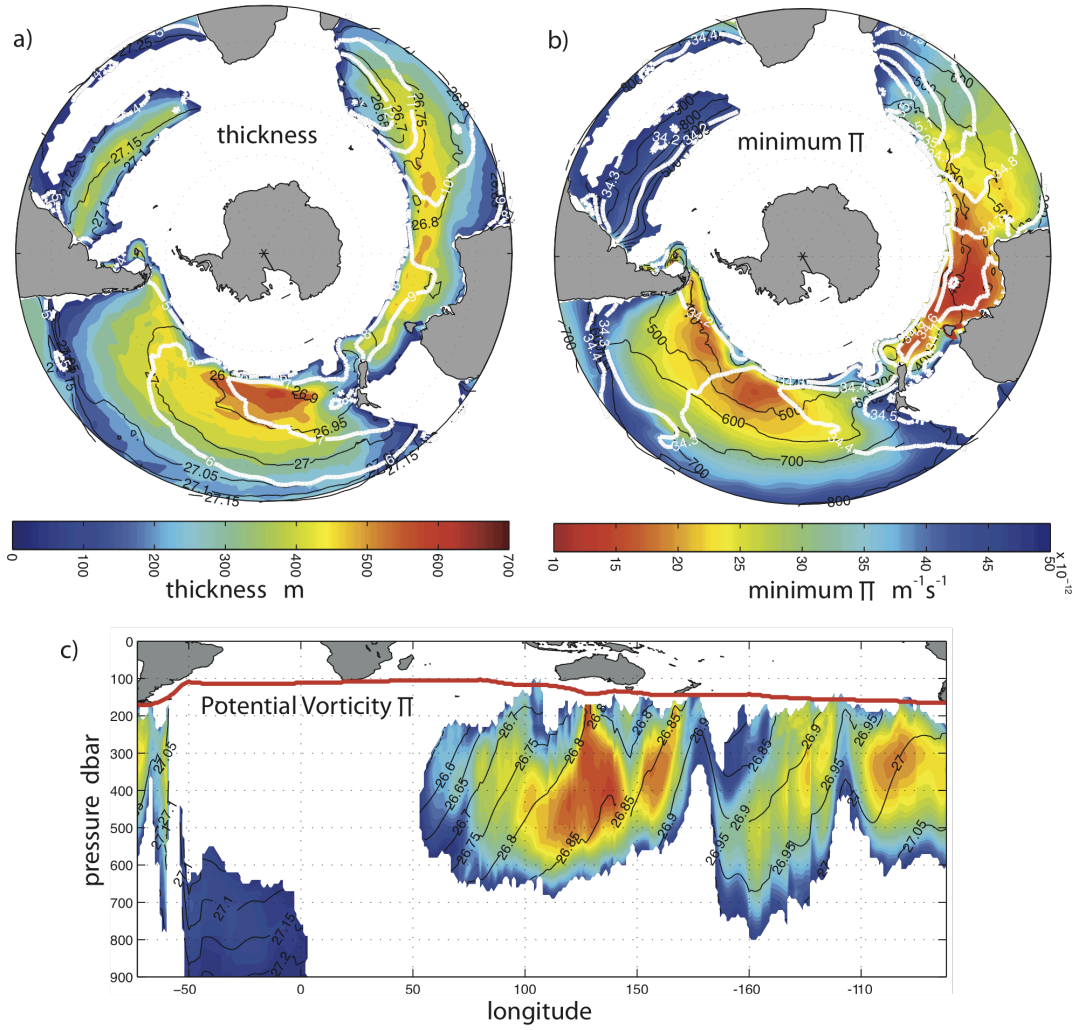


FIG. 1. (a) Annual mean thickness of Subantarctic Mode Water (SAMW). Core isopycnals and isotherms are superimposed in black and white contour lines, respectively. (b) Annual mean potential vorticity ( $\Pi$ ) of SAMW. Core isobars and isohalines are superimposed in black and white contour lines, respectively. (c) Section of annual mean  $\Pi$  of SAMW along the smoothed meridional  $\Pi$  minimum latitude with color scheme following (b). Location of that latitude indicated by red line on superimposed map. Black contour lines show isopycnals. Data only displayed for areas with  $|\Pi| < 50 \times 10^{-12} \text{ m}^{-1} \text{ s}^{-1}$  for more than four months out of 12.

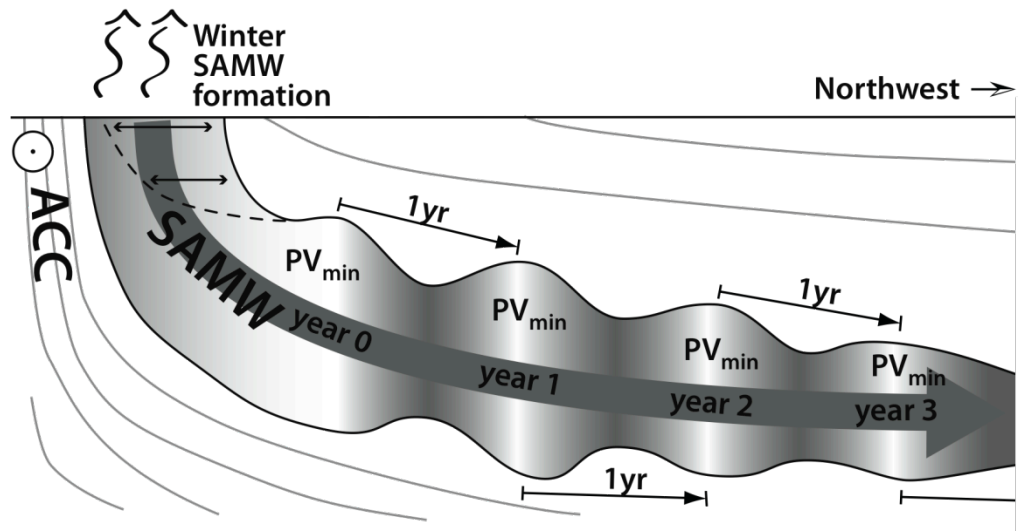


FIG. 2. Schematic of propagation of annually formed SAMW  $II$  minima anomalies propagating northwesterly from their source region at the base of the subtropical thermocline – proverbial  $II$  anomaly pigs in the SAMW python.

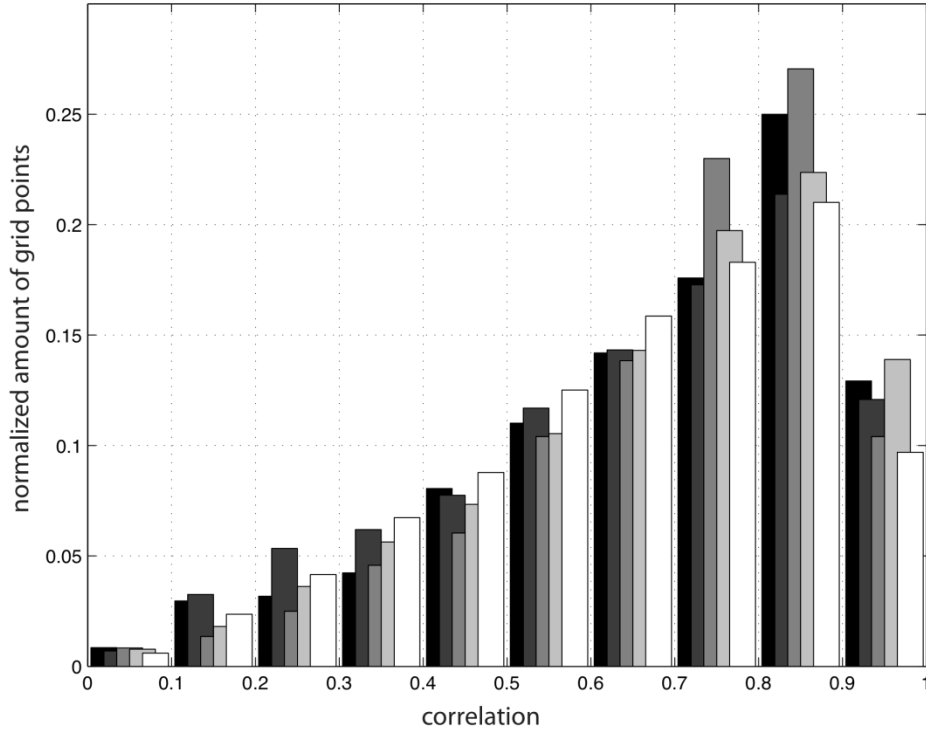


FIG. 3. Histogram of maximum correlation with the annual harmonic for each analyzed isopycnal area within the SAMW core, normalized by the total number of grid points for that isopycnal. Ordered from lightest Indian Ocean isopycnal in white ( $\sigma_\theta = 26.68 \text{ kg m}^{-3}$ ) successively to densest Pacific isopycnal in black ( $\sigma_\theta = 26.98 \text{ kg m}^{-3}$ ).

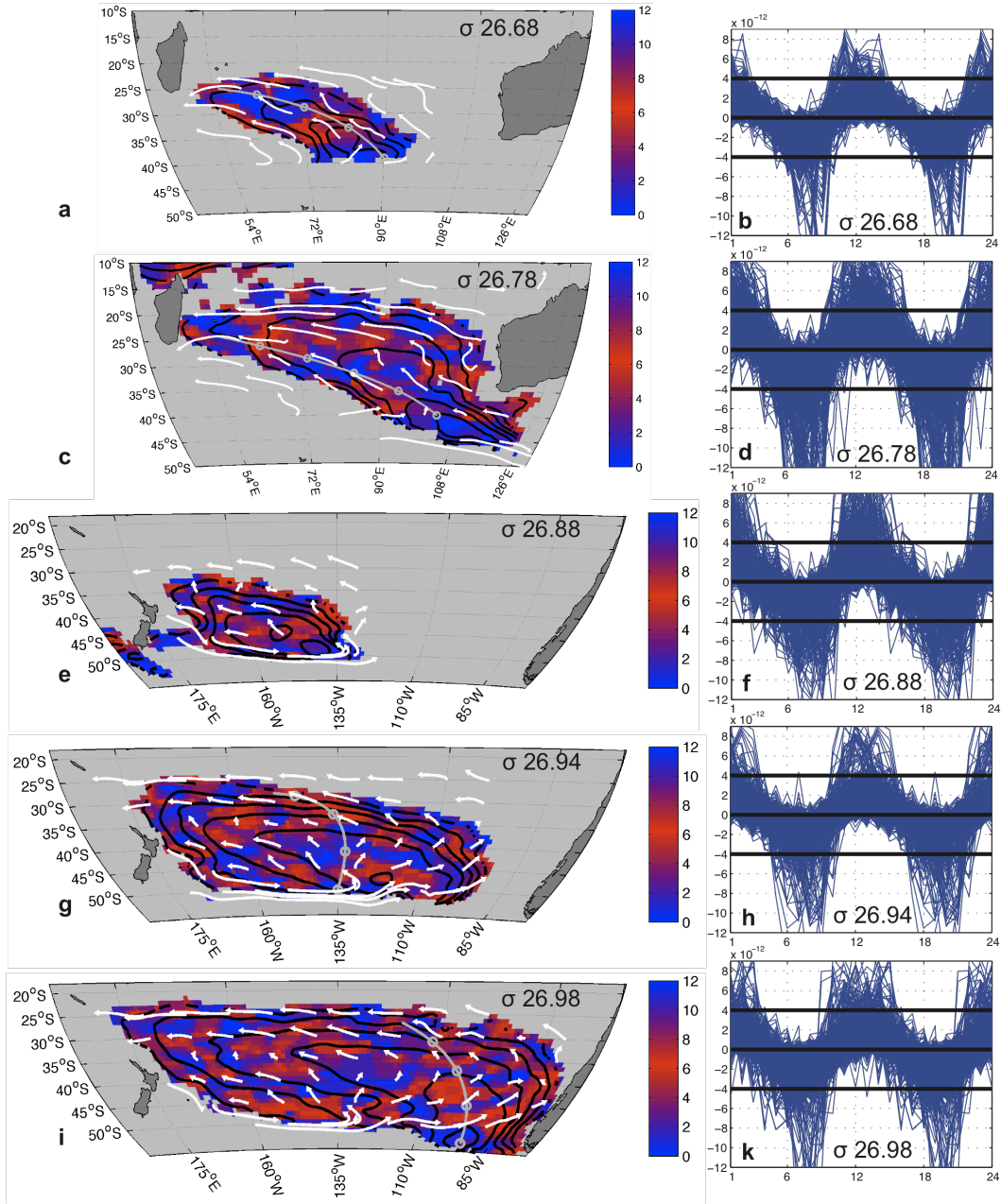


FIG. 4. Months of annual  $II$  minimum for five selected isopycnals in the Indian and Pacific Ocean in the left panels (a, c, e, g, i). Two-year geostrophic displacements are overlaid in white arrows as are  $II$  isolines at  $5 \times 10^{-12} \text{ m}^{-1} \text{ s}^{-1}$  intervals in black contours. An arrow with a length of  $5^\circ$  lat. represents a mean geostrophic current of  $\sim 0.9 \text{ cm s}^{-1}$ . Indicated in gray is the section analyzed in detail in Fig. 4, the circles mark every 1,000

km. Areas without year-round presence of SAMW are masked. Right panels (b, d, f, h, k) show the potential vorticity variability in the course of two successive climatological years for each  $1^\circ \times 1^\circ$  grid point in the corresponding left panel with correlation above 0.4. Each cycle is temporally shifted to its maximum correlation with an annual harmonic oscillation so that local phases match up for this global representation. The black lines at -4, 0 and  $4 (\times 10^{-12} \text{ m}^{-1} \text{ s}^{-1})$  are for reference purposes.



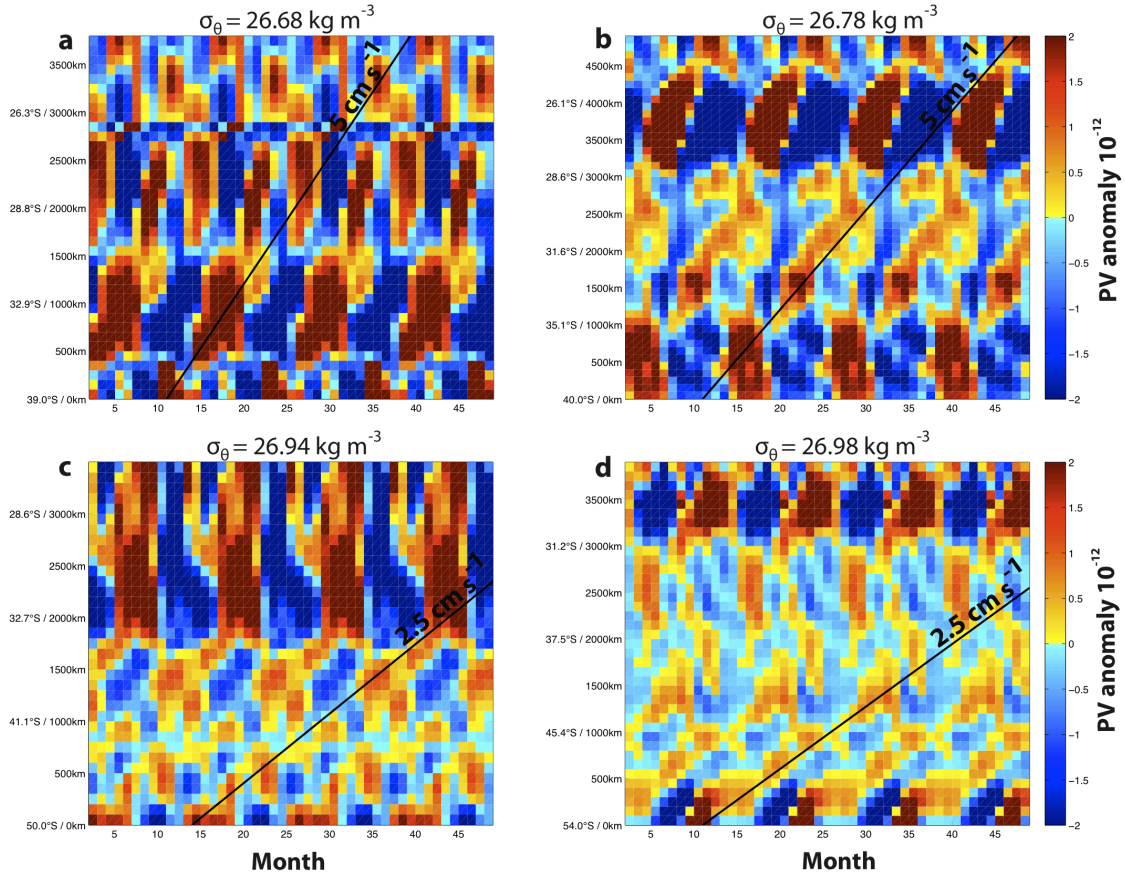


FIG. 5. Hovmöller diagrams of  $\Pi$  anomaly, thus  $\Pi$  seasonal cycle, along sections on four isopycnals, as indicated by gray lines in Fig. 4a, c, g, and i, respectively. Black lines reference the velocities indicated,  $5 \text{ cm s}^{-1}$  for the two Indian Ocean, and  $2.5 \text{ cm s}^{-1}$  for the two Pacific Ocean isopycnals.